Journal of Catalysis **198,** 296–308 (2001)
doi:10.1006/jcat.2001.3130, available online at http://www.idealibrary.com on IDEAL®

Characterization of Pd/MgO Catalysts: Role of Organometallic Precursor–Surface Interactions

Vladimiro Dal Santo,* Laura Sordelli,* Carlo Dossi,† Sandro Recchia,† Emiliano Fonda,‡,§ Gilberto Vlaic,‡,§ and Rinaldo Psaro*,[1]

*CNR Research Centre "CSSCMTBSO" and Dipartimento di Chimica Inorganica, Metallorganica e Analitica, Università degli Studi di Milano, Via Venezian 21, 20133 Milan, Italy; †Dipartimento di Scienze Chimiche, Fisiche e Matematiche, Università dell'Insubria, Via Lucini 3 22100 Como, Italy; ‡Dipartimento di Scienze Chimiche, Universita' di Trieste, Via L.Giorgieri 1, Trieste, Italy; and §Elettra S.p.A, Trieste, Italy

Received August 29, 2000; revised November 16, 2000; accepted November 18, 2000; published online February 8, 2001

$Pd(acac)_2$ was supported on a highly dehydroxylated and decarbonated magnesium oxide surface (MgO^{500}), on an untreated MgO surface (MgO^{AIR}), and on a silica (SiO_2^{450}). EXAFS and DRIFT data indicate that the organopalladium complex is adsorbed intact on all the surfaces, but its dispersion is dependent on the nature of the surface. On MgO^{500}, dispersion at the molecular level occurs, in contrast to the formation of islands of multilayers on MgO^{AIR} and SiO_2^{450}. The final properties of the metal phase, formed by H_2 treatment at 500°C, are dependent on precursor–surface interactions. HRTEM analysis shows a narrow distribution of the metal particles centered at 0.6 nm on MgO^{500}, and a wide diameter distribution around 6.1 and 9.9 nm on MgO^{AIR} and SiO_2^{450}, respectively. In the *n*-heptane dehydrocyclization at 500°C, the highest selectivity is shown by Pd/MgO^{500} catalysts and it is consistent with a predominant fraction of very small particles in close contact with surface basic sites.

Key Words: **palladium acetylacetonate; Pd/MgO; high-resolution transmission electron microscopy; extended X-ray absorption fine-structure spectroscopy; diffuse reflectance infrared Fourier transform spectroscopy; *n*-heptane dehydrocyclization.**

1. INTRODUCTION

Transition metal acetylacetonates have been used in the preparation of supported noble metal catalysts (1). Boitiaux *et al.* (2), using palladium acetylacetonate $Pd(acac)_2$ as a catalyst precursor, were able to prepare a Pd/γ-Al_2O_3 catalyst with a high degree of dispersion.

The surface chemistry of the adsorption of metal acetylacetonates is ruled by two mechanisms: (i) hydrogen bonding between the surface hydroxyl groups and the quasi-aromatic electron system of the acetylacetonate, and (ii) ligand exchange mechanism. In the latter mechanism, covalent bonding occurs and acacH is evolved. The adsorption is dependent on the geometry of the complex (such as the hydrogen bonding and the ability of the metal ion to accept a fifth ligand) and the acid–basic sites of the support. As proposed by Lesage-Rosemberg *et al.* (3), $Pd(acac)_2$ adsorbs on the alumina via a reaction with the OH groups leading to adsorbed Pd keeping one acac ligand. In contrast van Veen *et al.* (4) proposed the reaction only with c.u.s. Al^{3+}, with transfer of the acac ligand to Al^{3+}.

The use of basic support materials for noble metals catalysts has become the subject of increased attention (5). The high aromatization selectivity of nonacidic Pd/MgO catalysts was also observed in our laboratory and it was reported that catalysts prepared by chemical vapor deposition of an organometallic precursor proved to be very active (6).

An easier alternative route to chemical vapor deposition is the chlorine-free solvent impregnation of $Pd(acac)_2$ on MgO, which allows removal of the bifunctional reforming behavior related to the formation of acidic Mg^{2+} Cl^- sites and collapse of the activity due to chlorine atoms chemisorbed on Pd particles (7). The use of this molecular precursor is particularly promising in this sense, since the metallic phase can be obtained by heating the adsorbed precursor in a stream of hydrogen, avoiding calcination.

It is well known that direct interaction between an organometallic precursor and the surface active sites of an inorganic oxide is highly dependent on the pretreatment of the surface itself (dehydration, dehydroxylation, decarbonatation, absence of oxygen, etc.) (8). In the present work we present our detailed investigation of the structural characterization of the surface chemistry of $Pd(acac)_2$ resulting from solvent impregnation with different magnesia surfaces together with the final properties of supported particles as determined by EXAFS, DRIFT/FTIR spectroscopies, and high-resolution transmission electron microscopy (HRTEM).

2. EXPERIMENTAL

2.1. Catalyst Preparation

$Pd(acac)_2$ was synthesized in our laboratory according to the literature procedure (9). The MgO support material (Merck, 97%, Batch No. 308 TA 390565) was refluxed in

[1] E-mail: rpsaro@csmtbo.mi.cnr.it. Fax: +39-022362748.

0021-9517/01 $35.00

deionized water for 3 h and then dried in air overnight at 110°C. This treatment results in an increase in surface area to 300 $m^2\ g^{-1}$. This support is referred to as MgO^{AIR}. Highly dehydroxylated and decarbonated magnesium oxide (MgO^{500}) was obtained by heating MgO^{AIR} from 25 to 500°C in air and further evacuating ($P = 10^{-5}$ mbar) at this temperature overnight. The SiO_2 support (Grace Davison 62, surface area 214 m^2/g) was stirred for 3 h in 0.1 M HNO_3, washed to neutrality, and then dried overnight at 110°C. Prior to impregnation the SiO_2 was treated with the procedure outlined for MgO^{500} but at 450°C (SiO_2^{450}).

Toluene (Aldrich, HPLC-grade, 99.8%) was dried over activated molecular sieves in an inert atmosphere.

The oxide supports were impregnated at room temperature under an argon atmosphere with a diluted solution of $Pd(acac)_2$ in anhydrous toluene, obtaining a 2 wt% metal loading for each sample, as determined by AAS after dissolution of the catalyst in a HCl/HNO_3 mixture. On MgO^{500} the impregnation solution became colorless after a few hours of stirring; the yellow impregnated material was then filtered off, and dried overnight *in vacuo* (10^{-2} mbar). On all the other supports the solution remained light yellow after 24 h of stirring. The solvent was removed *in vacuo*, and the sample dried overnight *in vacuo*. Finally the impregnated catalysts were treated in flowing hydrogen (50 ml/min) from 25 to 500°C, at 10°C/min, and kept at 500°C for 1 h.

2.2. Infrared Studies

Spectra were recorded on a Digilab FTS-40 equipped with a KBr beamsplitter and a DTGS detector operating between 400 and 4000 cm^{-1}.

Transmission spectra were recorded on pellets obtained by pressing the powder oxide supports at 5 ton cm^{-2}, thermally pretreated according to the procedure reported in Section 2.1. The pellets were then impregnated *in situ*, with a toluenic solution of $Pd(acac)_2$, and finally dried in vacuo for 6 h. The technique of impregnation and of working up to obtain IR spectra of supported organometallic compounds in the complete absence of air and moisture has been described elsewhere (10).

DRIFT spectra of the sample powder were recorded using a Harrick reaction chamber with KBr and ZnSe windows and a Harrick DRA-2C1 accessory. The catalysts were placed in the cell sample holder under an inert atmosphere. The cell was connected to a vacuum gas line for the sample treatment and to a programmable heater operating from ambient temperature to 450°C.

For $Pd(acac)_2/SiO_2^{450}$ only the transmission spectrum was recorded, as the strong absorption from the support in the DRIFT spectra masks the ligand bands and any attempt at subtraction is ineffective. For $Pd(acac)_2/MgO^{AIR}$ it was impossible to register any significant spectra due to strong absorption of the surface carbonates in the spectral region characteristic of the acetylacetonate ligand.

2.3. Temperature-Programmed Studies

The kinetics of the thermal decomposition to metal of the supported $Pd(acac)_2$ were studied by temperature-programmed reductive decomposition (TPRD). A detailed description of the instrumental setup is reported elsewhere (11). Typical conditions are: 100 mg of catalysts, flowing gas mixture of 4.92% H_2 in He (10.3 ml/min) flow, heating rate of 3°C/min from 25 to 500°C. The choice of mass channels to be monitored was optimized to discriminate between 2,4-pentandione, 2,4-pentandiol, 2-propanone, 2-propanol, ethane, and methane. Temperature-programmed reduction (TPR) of Pd/MgO^{500} was carried out on a modified Micromeritics Pulse Chemisorb 2700 apparatus under standard conditions (12).

2.4. EXAFS Studies and Data Analysis

X-ray absorption spectra were collected at the XAS-13 beamline of LURE (Orsay, France) operating at 2 GeV of positron energy and at a storage ring current of 200 mA. The experimental station was equipped with a Si(331) channel-cut crystal monochromator. Second harmonics are absent due to the the extinction rule of the Si(331); third harmonics are neglectable due to the low photon flux at that energy. Pd metal foil was used for the angle/energy calibration.

All spectra were recorded at 25°C in transmission mode at the Pd *K* edge (24.35 keV) over the range 24.2–25.4 keV, with a sampling step of 3 eV and an integration time of 2 s for each point. Incident and transmitted photon fluxes were detected with ionization chambers filled, respectively, with 0.1 and 0.4 bar of Kr. Each spectrum was acquired five times for the best minimization of the noise and estimation of the fit error bars through the experimental standard deviation (13).

The powder samples were loaded under an inert atmosphere in the catalysis-EXAFS cell (Lytle type). Sample homogeneity was checked by taking low-exposure photographs of the samples. The spectra of $Pd(acac)_2/MgO^{500}$, $Pd(acac)_2/MgO^{AIR}$, and $Pd(acac)_2/SiO_2^{450}$ were recorded after each of the following steps: impregnation; *in situ* reduction at 500°C; *in situ* oxidation at 500°C of the reduced sample; *in situ* reduction of the calcined sample.

Single-scattering data analysis was performed with EXAFS pour le Mac (14) software. Experimental $\chi(k)$ data were extracted from the absorption data by a conventional procedure (linear pre-edge background subtraction; fifth polynomial fit for the atomic-like contribution, subtracted following the procedure proposed by Lengeler and Eisenberger (15); normalization to edge height). The k^3-weighted $\chi(k)$ data were Fourier transformed (Kaiser window, $\tau = 2.5$) in a typical k range of 3–14 $Å^{-1}$, and the main contributions to the Fourier transform modulus were filtered to obtain metal nearest-neighbor shells. The so obtained filtered contributions were analyzed using

the nonlinear least-squares fitting programs developed by Michalowicz (16). Experimental phase shift and amplitude functions of the scattering atoms were used in the single-scattering fit of the MgO-supported samples.

Analysis of the just impregnated samples was performed also by including simulation of the multiple scattering contributions present in the signals. For this analysis the FEFF7 program package (17) was used, which calculates, starting from a model structure, all the theoretical signals produced by all the single- and multiple-scattering paths. The fits were performed on the unfiltered k^1- and k^3-weighted spectra, keeping fixed the coordination numbers. Scattering paths were included up to the distance of 4.5 Å, because no signal was detectable in the FFT of any samples beyond $R = 4$ Å. Paths with relative amplitude lower than 6% were neglected.

2.5. HRTEM Micrographs

At the end of the reduction treatment the catalysts were further ground and the powders were dispersed in *n*-heptane and disintegrated ultrasonically. Drops of the resulting suspensions were deposited on holey carbon grids which, after evaporation of the solvent, were inserted into the sample compartment of a JEOL 2000EX high resolution transmission electron microscope. Micrographs of each sample were taken at low (×150,000–250,000) and high (up to ×800,000) magnification to have a complete map of every magnesia grain. The metal particle distribution versus diameter for each sample was obtained for at least 300 counts.

2.6. Catalytic Studies

The dehydrocyclization of *n*-heptane was performed at 500°C in a continuous-flow, fixed-bed microreactor, working at atmospheric pressure, with a H_2/C_7H_{16} ratio of about 20. Quantitative analyses of reactants and products were carried out on an on-line gas chromatograph (Carlo Erba Instruments HRGC 5160) fitted with a thermostated sampling valve and a flame ionization detector, using a 50-m × 0.2-mm crosslinked methylsilicone (Hewelett–Packard PONA) capillary column.

At the end of the catalytic test, the model regeneration procedure was conducted in two steps: (i) heating in flowing oxygen from 25 to 400°C at 10°C/min and keeping at this temperature for 1 h; (ii) cooling down to 25°C in flowing argon, reducing in flowing hydrogen from 25 to 500°C at 10°C/min, and keeping at 500°C for 1 h.

3. RESULTS

3.1. IR and DRIFT Spectra

DRIFT and transmission FTIR investigations of $Pd(acac)_2$ chemisorbed on MgO^{500} were carried out in the region 1800–1100 cm^{-1} (Figs. 1b, 1c) on powder and pellet samples, respectively (see Section 2.2). A mechanical mixture obtained by grinding, under inert atmosphere, the palladium precursor and the MgO^{500} was used as a reference model DRIFT spectrum to compensate the matrix effect of the support (Fig. 1a).

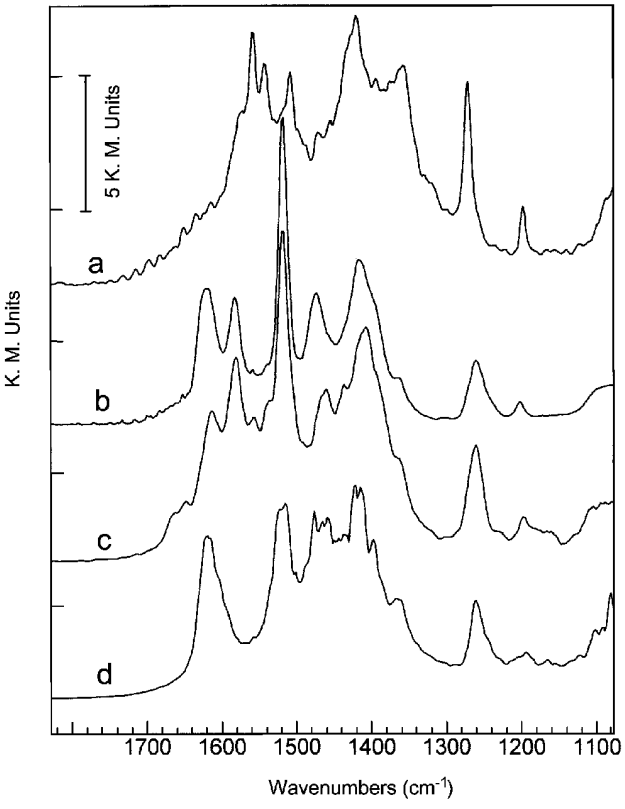

FIG. 1. IR spectra in the 1800–1100 cm^{-1} region of $Pd(acac)_2$ on MgO^{500}: (a) DRIFT spectrum of a mechanical mixture of $Pd(acac)_2$ and MgO^{500}; (b) transmission spectrum of $Pd(acac)_2$ chemisorbed on MgO^{500} as pellet; (c) DRIFT spectrum of $Pd(acac)_2$ chemisorbed on MgO^{500} as powder; (d) DRIFT spectrum of acacH/MgO^{500} as powder.

The DRIFT spectrum of acacH adsorbed on MgO^{500} was recorded to follow the presence of the surface reaction between the ligand and the basic OH, O^{2-} groups and/or the c.u.s. Mg^{2+} Lewis acid sites (Fig. 1d).

The band assignment, reported in Table 1, was made by comparing the recorded spectra with that of the pure compound available in the literature (18). The multiplicity of the bands does not change with respect to the pure compound spectrum, either in the spectrum of the mechanical mixture (Fig. 1a) (apart from the $\delta(CH_3)_{as}$) or in the spectrum of the chemisorbed compound (Fig. 1c); the latter shows quite large shifts for the bands ascribed to the symmetric stretching of C–O and to the double overtone of o.o.p. bending of C(3)–H, respectively +58 and +41 cm^{-1}, tacking the former as a reference.

The spectrum of the pellet (Fig. 1b) is quite similar to that of the powder, the major difference being represented by the position of $\delta(CH_3)_s$.

TABLE 1

Assignment of IR Bands in the Region 1800–1100 cm^{-1} for Various $Pd(acac)_2/MgO^{500}$ Samples

Powder[a]	Pellet[b]	Mechanical mixture[c]	acacH/MgO^{500}[d]	Assignment
1614 (m)	1618 (m)	1556 (vs)	1619 (s)	$\nu(C{=}O)_s$
1582 (s)	1583 (m)	1541 (s)	[e]	$2\gamma(C{-}H)$
1519 (vs)	1517 (vs)	1510 (s)	1518 (vs)	$\nu(C{=}C{-}C)_{as}$
1461 (m)	1473 (m)	[e]	1474 (s)	$\delta(CH_3)_{as}$
1437 (m)	[e]	[e]	[e]	$\delta(CH_3)_{as}$
1408 (m)	1417 (m)	1422 (vs)	1419 (vs)	$\nu(C{-}O)_{as}$
1361 (sh-w)	1342 (sh-w)	1361 (s)	1366 (sh-m)	$\delta(CH_3)_s$
1261 (m)	1261 (m)	1272 (s)	1261 (m)	$\nu(C{=}C{-}C)_s$
1198 (w)	1202 (w)	1197 (w)	1195 (w)	$\beta(C{-}H)$

[a] DRIFT measurements.
[b] Transmission FT-IR measurements.
[c] DRIFT of mechanical mixture of $Pd(acac)_2$ and MgO^{500}.
[d] DRIFT data of MgO^{500} impregnated with toluenic solution of acacH.
[e] Not observable.

TABLE 2

Transmission FTIR Spectrum Band Wavenumbers and Assignation of the $Pd(acac)_2/SiO_2$ Sample and of the $Pd(acac)_2$–SiO_2 Mechanical Mixture

Reference[a]	Pellet[b]	Assignment
1571 (Vs)	1558 (m)	$\nu(C{-}O)_s$
1550 (Vs)	absent	$2\gamma(CH)$
1525 (Vs)	1525 (Vs)	$\nu(C{-}C{-}C)_{as}$
1379 (s)	1384 (m)	$\nu(C{-}O)_{as}$
1358 (m)	absent	$\delta(CH_3)_s$
1272 (m-sh)	1269 (vw)	$\nu(C{-}C{-}C)_s$
1198 (w)	[c]	$\beta(C{-}H)$
1022 (s)	1020 (Vs)	$\rho(CH_3)$
936 (m)	940 (w-sh)	$\nu(C{-}CH_3)$
785 (s)	[c]	$\gamma(C{-}H)$
699 (m)	705 (vw)	βring
677 (m)	686 (vw)	γring
660 (w)	666 (vw)	βring
465 (s)	501 (w)	$\nu(MO_4)$

[a] Mechanical mixture of $Pd(acac)_2$ and SiO_2^{450}.
[b] SiO_2^{450} pellet impregnated with $Pd(acac)_2$ toluenic solution.
[c] Not observable, falling under absorption bands of silica.

Spectra of $Pd(acac)_2/MgO^{500}$ and acacH/MgO^{500} (Fig. 1d) are quite similar. The band relative to the double overtone of C–H bond stretching is absent in the acacH/MgO^{500} spectrum, and the band attributed to the symmetric CH_3 bending is shifted to higher wavenumber.

When $Pd(acac)_2$ was supported on a weakly acidic surface such as SiO_2^{450} some more relevant differences occurred in the region 1600–1200 cm^{-1} (Fig. 2a) with respect to the spectrum of the mechanical mixture (Fig. 2a). Other than small entity shifts, two bands at 1550 and 1358 cm^{-1} were not present any more. The band assignment is reported in Table 2.

3.2. *Temperature-Programmed Studies*

The thermochemical behavior under reducing conditions of $Pd(acac)_2$ pure and adsorbed onto different magnesium oxide surfaces (MgO^{500}, MgO^{AIR}) has been previously

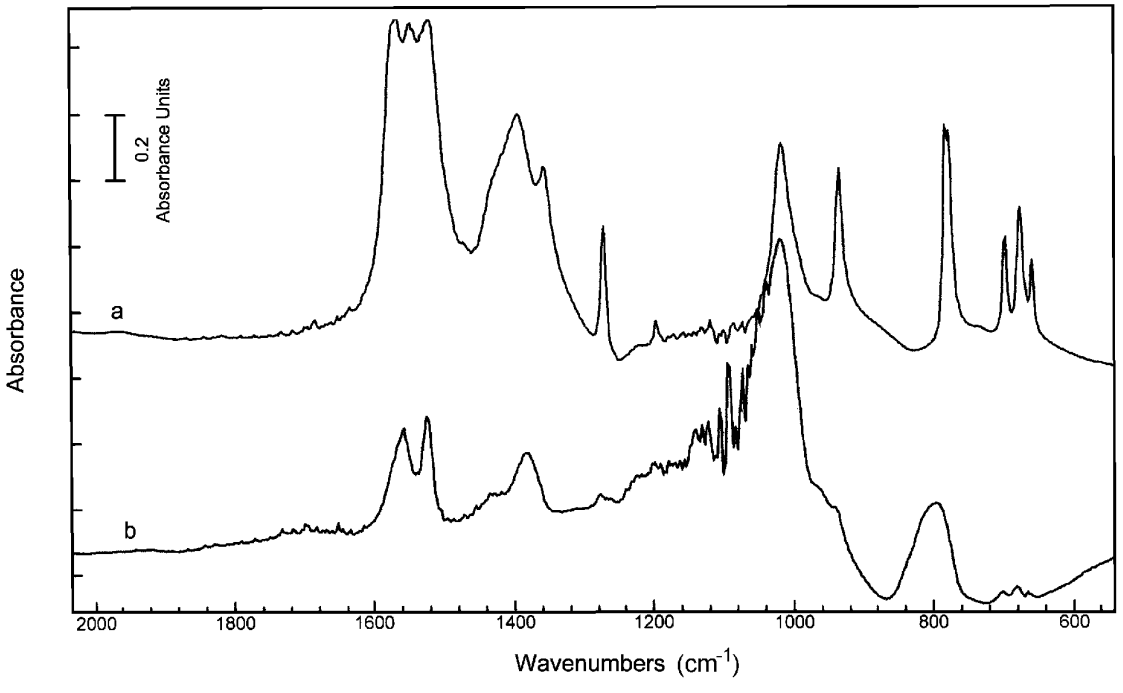

FIG. 2. Transmission FTIR spectra of $Pd(acac)_2$ supported on SiO_2^{450}: (a) mechanical mixture; (b) impregnated sample.

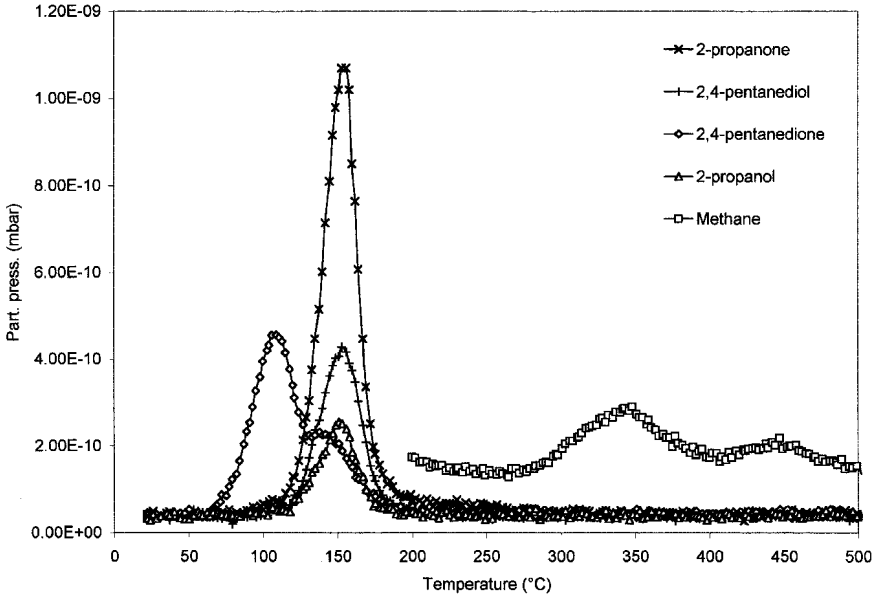

FIG. 3. TPRD profile of $Pd(acac)_2/SiO_2^{450}$.

reported (19). The TPRD profile of $Pd(acac)_2/SiO_2^{450}$ is shown in Fig. 3. A single peak was observed at 110°C, indicative of the evolution of 2,4-pentanedione. A second group of peaks of hydrogenation products (2,4-pentanediol, 2-propanol, 2-propanone) were centered at about 155°C. At higher temperature, ca. 350°C, an additional evolution peak, due to methane formation, was observed.

The TPR profile (12) of reduced–calcined $Pd(acac)_2/MgO^{500}$ shows a single hydrogen consumption peak below 170°C, the observed H/Pd ratio is 98.2% of the value corresponding to the stoichiometric reduction from PdO to metallic Pd.

3.3. *EXAFS Data*

Adsorption state of Pd(acac)$_2$ on different oxide surfaces. The $\chi(k)$ spectra of the $Pd(acac)_2/MgO^{500}$, $Pd(acac)_2/MgO^{AIR}$, and $Pd(acac)_2/SiO_2^{450}$ systems freshly impregnated and of the pure $Pd(acac)_2$ complex have been extracted with the same procedure in the k range 2.5–12.2 $Å^{-1}$. Comparison of the moduli and imaginary parts of the Fourier transformed spectra immediately proves the similarity of the $Pd(acac)_2/MgO^{AIR}$, and $Pd(acac)_2/SiO_2^{450}$ impregnated samples to the pure precursor, while the MgO^{500}-supported system shows a global intensity reduction and a modified imaginary part for the higher shell peaks. When considering the structure of the higher shells from the acetylacetonate rings surrounding the absorbing atom in the precursor complex, the contribution to the signal from multiple-scattering paths cannot be neglected. In the following, the ligand carbon atoms corresponding to the $-C{=}O$, $-CH$, and $-CH_3$ groups are denoted C_1, C_2, and C_3, respectively. The use of a theoretical model built up from the crystallographic data of $Pd(acac)_2$ crystal in the FEFF7 program provided excellent agreement with the experimental signals of the pure complex, also allowing detection of the small contributions from the C_1 carbon atoms belonging to adiacent molecules at 3.37 Å. In fact, significant improvement in the reduced χ^2 function (28.6 vs 41.6 for 11 free parameters) is achieved by including in the fit the contributions of the paths involving such atoms. The same result is obtained for the MgO^{AIR}- and SiO_2- supported samples, suggesting the existence of crystallites on the support surface produced during impregnation. No contribution, however, is detectable in both EXAFS spectra from the Pd atoms of adiacent molecules, in the crystal present at 5.14 Å, because of the dumping of the signal above 4.5 Å due to thermal and static disorder effects.

On impregnation on the MgO^{500}, the complex dispersion seems to occur at molecular level, as the inclusion of intramolecule paths does not affect the fit quality. Moreover, geometrical distortions of the acetylacetonate rings around the Pd atoms can be inferred from the increase in the Pd–O and $Pd–C_1$ distances and the decrease in the $Pd–C_2$ distance (Table 3). A relevant increase in the Debye–Waller factors relative to the $Pd–C_1$, $Pd–C_2$, $Pd–O–C_1$, $P–O–C_2$, $Pd–O–C_3$, and O–Pd–O paths further suggests a wide distribution in the ring distortion degree. Any attempt to include contributions from surface oxygen or Mg atoms was of no statistical significance. In Fig. 4 are shown the experimental and best-fit theoretical EXAFS and FT spectra obtained from the multiple-scattering calculation for $Pd(acac)_2/MgO^{500}$ and $Pd(acac)_2/MgO^{AIR}$ when the contribution to the total signal from all the significant paths is included. The fit results of the impregnated samples are reported in Table 3.

TABLE 3

Principal Path Contribution in Multiple Scattering Curve-Fitting Results of the Pd *K*-Edge EXAFS Spectra of Impregnated Samples

Sample	Path	Degen	R (Å)	$\Delta\sigma$ (Å)	ΔE_0 (eV)
$Pd(acac)_2/MgO^{AIR}$	Pd–O	4	1.960 ± 0.002	0.072 ± 0.002	0.52 ± 0.05
	Pd–C_1	4	2.898 ± 0.002	0.037 ± 0.002	0.52 ± 0.05
	Pd–O–C_1	8	3.083 ± 0.002	0.045 ± 0.002	0.52 ± 0.05
	Pd–C_2	2	3.191 ± 0.002	0.101 ± 0.002	0.52 ± 0.05
$Pd(acac)_2/MgO^{500}$	Pd–O	4	2.021 ± 0.002	0.076 ± 0.018	0.55 ± 0.05
	Pd–C_1	4	2.964 ± 0.002	0.088 ± 0.002	0.55 ± 0.05
	Pd–O–C_1	8	3.154 ± 0.002	0.098 ± 0.002	0.55 ± 0.05
	Pd–C_2	2	3.164 ± 0.002	0.120 ± 0.002	0.55 ± 0.05

After activation treatment. The EXAFS spectra of $Pd(acac)_2/MgO^{500}$, $Pd(acac)_2/MgO^{AIR}$ and $Pd(acac)_2/SiO_2^{450}$ recorded after *in situ* reduction in H_2 flow are shown in Fig. 5, which also presents comparison of the moduli of the Fourier transformed spectra between the two MgO-supported samples after reduction and of the pure Pd metal foil.

In the Pd/MgO^{500} sample two well-resolved peaks are present, coming from a Pd–O shell and a Pd–Pd shell. The two-shell single-scattering best fit on the filtered range 1.1–3.1 Å provided 2.0 oxygen atoms at 1.98 Å and 4.7 Pd neighbors at a distance slightly shorter than in the first Pd metal shell (2.73 Å vs 2.75 Å). The experimental phase and amplitude functions for Pd and O atoms were extracted from the spectra of the reference samples Pd foil, PdO, and pure $Pd(acac)_2$ complex (Table 4).

The Pd/MgO^{AIR} sample after reduction shows a first peak due to an oxygen shell and a more complex structure that can be properly fitted only as a contribution of three Pd overlapping shells. The four-shell best fit of the filtered peaks in the range 1.1–4.0 Å gives two oxygen atoms at 1.97 Å, four Pd neighbours at 2.74, four at 3.38 and three at 3.85 Å. The four-shell fit requires a total of 16 parameters

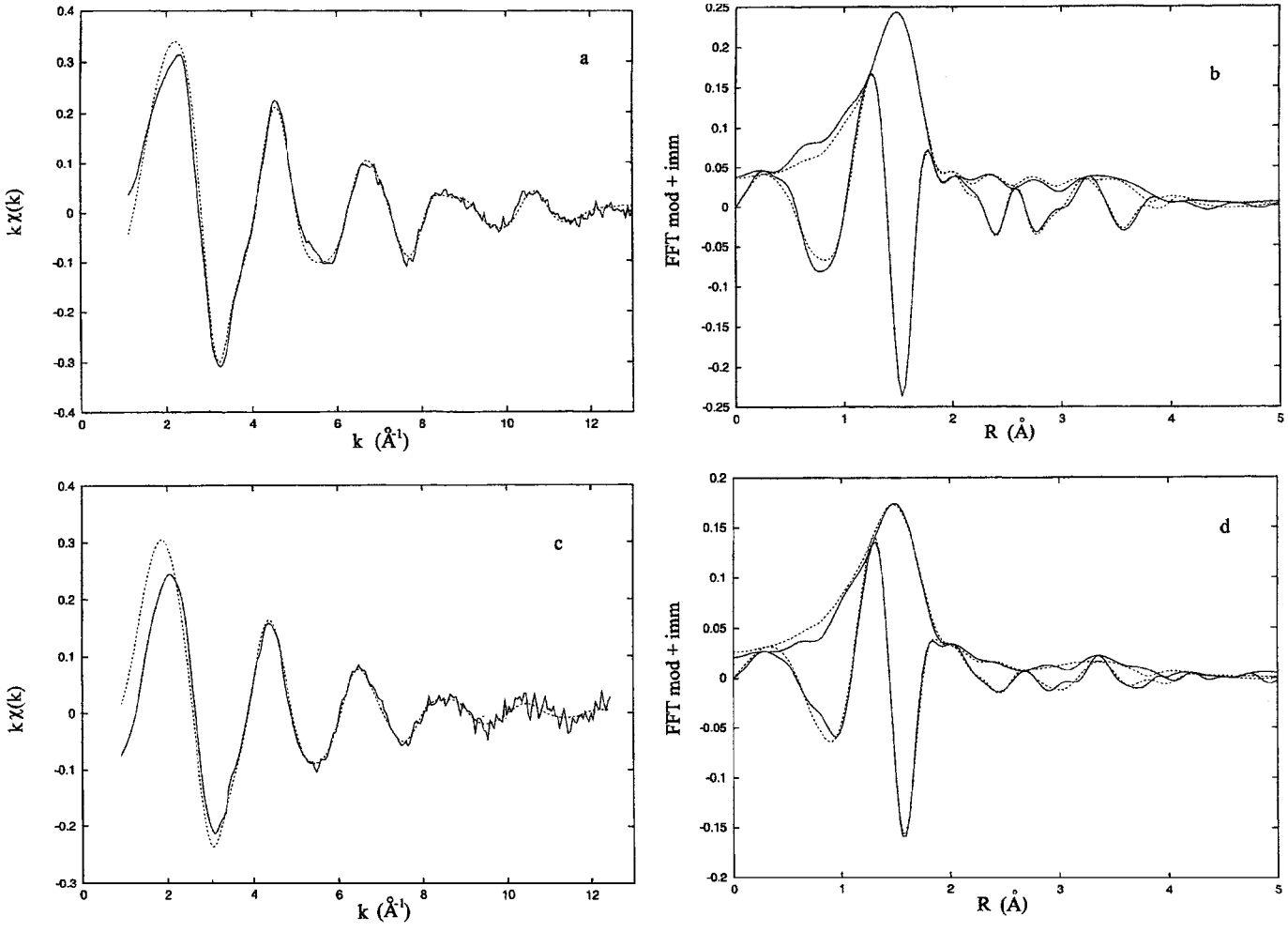

FIG. 4. Experimental (dotted line) and best-fit theoretical (solid line) EXAFS and FT spectra obtained from the multiple scattering calculation for $Pd(acac)_2/MgO^{500}$ (a, b) and $Pd(acac)_2/MgO^{AIR}$ (c, d).

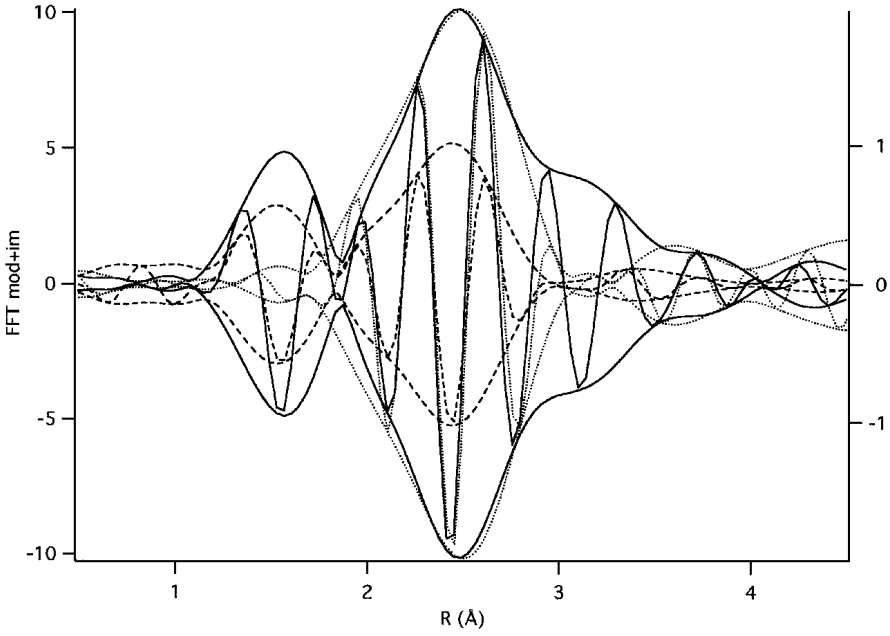

FIG. 5. Comparison of the moduli and imaginary parts of Fourier spectra of $Pd(acac)_2/MgO^{500}$ (dashed line) and $Pd(acac)_2/MgO^{AIR}$ (solid line) recorded after *in situ* reduction in H_2 flow together with the pure Pd metal foil (dotted line).

out of 20 *df*, and the fit converges to the same values either by letting all the parameters vary together or by fixing some constraints so to reduce the number of free parameters. The statistical significance of the shell addition has been positively checked with the *F* test (20). The Pd–Pd distances were found to correspond to the first two Pd shells in Pd foil and to the first Pd shell in PdO. The coordination numbers indicate that about one-half of the Pd atoms have the Pd oxide coordination, and the remaining are in the form of large metal particles.

After reduction at 500°C the Pd/SiO_2^{450} sample shows no Pd–O contribution and the first peak best fit consists of nine nearest Pd neighbors at 2.75 Å. The first shell distance and coordination number suggest the existence of metal particles larger than those obtained on MgO^{500}. Moreover, the features of the peaks at longer distance well reproduce the contributions of the higher shells of the foil, confirming the formation of large Pd particles with the fcc structure of Pd metal. A complete list of the parameters obtained by the fitting of the reduced sample spectra is given in Table 5.

TABLE 4

Crystallographic Parameters of Reference Compounds Used in the Single-Scattering Analysis

Sample	Shell	*N*	*R* (Å)	σ (Å)[a]
Pd foil	Pd	12	2.75	0.07
	Pd	6	3.89	
PdO	O	4	2.02	0.07
	Pd	4	3.03	
	Pd	8	3.42	
$Pd(acac)_2$	O	4	1.963	0.07

[a] Arbitrary values used in experimental amplitude function extraction.

The calcination in oxygen flow after the reduction treatment produces Pd oxide phases on both activated and nonactivated magnesia (Table 5). For the reduced–calcined Pd/MgO^{AIR} sample the FT spectrum coincides perfectly with that of the pure oxide, suggesting the presence of massive oxide particles. For the Pd/MgO^{500} sample the oxygen peak at the distance of 2.02 Å is originated by four nearest oxygen neighbors, but the second shell contribution is lower with respect to the pure bulk oxide.

The $Pd(acac)_2/MgO^{500}$ sample, on undergoing a second reduction following the calcination, shows the contributions of 2.4 oxygen atoms at 2.01 Å and 4.2 Pd atoms at 2.73 Å, which means that there are no structural differences around the absorbing atoms with respect to the first reduction, within experimental error, there still being present very small metal particles interacting with the support oxygen atoms.

$Pd(acac)_2/MgO^{AIR}$ after the second reduction still shows the large peak due to the overlap of three Pd shells, but the intensity of the higher Pd distance contribution is now lower compared with the first reduction and the oxygen shell is less intense. Three Pd shells and one of oxygen are necessary to obtain a good fit, in agreement with the coexistence of metal and oxide particles, but the contribution from metal fcc palladium (first and third Pd shells) is now more relevant with respect to the oxide contribution (oxygen and second Pd shells), as reported in Table 5.

TABLE 5

Single Scattering Curve-Fitting Results of the Pd *K*-Edge EXAFS Spectra Recorded at the End of *in Situ* Treatments

Sample	Treatment	Shell	CN[a]	R (Å)[b]	$\Delta\sigma$ (Å)[c]	ΔE_0 (eV)
Pd/SiO_2^{450}	H_2	Pd	9.2 ± 0.4	2.753 ± 0.002	0.072 ± 0.002	0.6 ± 0.2
Pd/MgO^{500}	H_2	O	2.0 ± 0.2	1.980 ± 0.006	0.089 ± 0.012	-2.9 ± 0.6
		Pd	4.7 ± 0.3	2.729 ± 0.006	0.091 ± 0.0036	-5.5 ± 0.7
Pd/MgO^{AIR}	H_2	O	1.9 ± 0.3	1.980 ± 0.009	0.061 ± 0.002	-2.7 ± 1.7
		Pd	3.8 ± 0.7	2.737 ± 0.008	0.059 ± 0.009	-1.8 ± 1.4
		Pd	4.2 ± 0.9	3.38 ± 0.01	0.075 ± 0.003	-6.9 ± 1.4
		Pd	3.0 ± 0.1	3.85 ± 0.04	0.087 ± 0.002	-0.1 ± 3.4
Pd/MgO^{500}	H_2–O_2	O	4.5 ± 0.4	2.02 ± 0.01	0.081 ± 0.009	2.2 ± 1.0
		Pd	2.6 ± 0.6	3.086 ± 0.008	0.075 ± 0.003	2.5 ± 1.4
		Pd	3.1 ± 0.9	3.362 ± 0.008	0.089 ± 0.005	4.5 ± 1.7
Pd/MgO^{AIR}	H_2–O_2	O	4.2 ± 0.4	2.015 ± 0.006	0.064 ± 0.002	2.1 ± 0.6
		Pd	4.0 ± 0.5	3.086 ± 0.008	0.068 ± 0.004	0.9 ± 0.3
		Pd	8.0 ± 0.8	3.468 ± 0.009	0.093 ± 0.009	-2.3 ± 1.4
Pd/MgO^{500}	H_2–O_2–H_2	O	2.4 ± 0.1	2.016 ± 0.006	0.085 ± 0.009	-2.3 ± 0.6
		Pd	4.2 ± 0.3	2.730 ± 0.006	0.091 ± 0.003	-4.3 ± 0.5
Pd/MgO^{AIR}	H_2–O_2–H_2	O	1.7 ± 0.3	1.98 ± 0.01	0.0825 ± 0.0146	-0.9 ± 2.0
		Pd	6.5 ± 0.6	2.748 ± 0.003	0.0738 ± 0.048	-2.6 ± 0.5
		Pd	2.7 ± 1.4	3.42 ± 0.01	0.0712 ± 0.0288	-2.2 ± 0.2
		Pd	1.2 ± 1.3	3.89 ± 0.04	0.0531 ± 0.0713	-2.4 ± 5.3

[a] Coordination number.
[b] Interatomic distance.
[c] Debye–Waller factor, σ = root-mean-square internuclear separation.

3.4. HRTEM Results

In Fig. 6 are shown the histograms of the Pd particle size distribution for freshly reduced Pd/MgO^{500}, Pd/MgO^{AIR}, and Pd/SiO_2^{450} samples, as measured on high-resolution HRTEM transmission electron micrographs, which exibit a uniform particle dispersion over all the support grains. A narrow distribution centered at about 0.6 nm is found

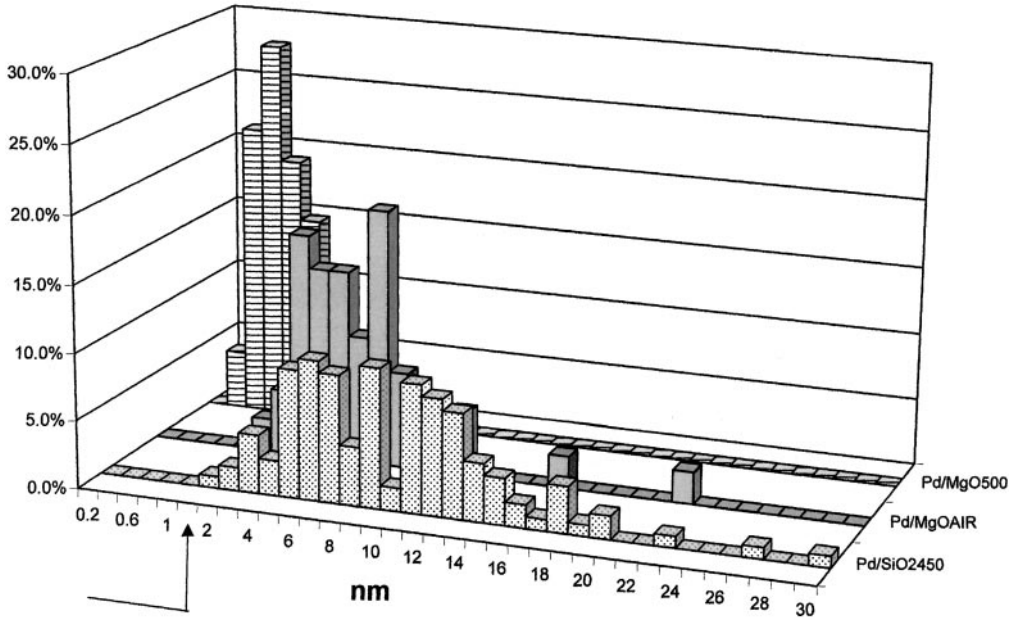

FIG. 6. Histograms of the Pd particle size distribution for Pd/MgO^{500}, Pd/MgO^{AIR}, and Pd/SiO_2^{450} as measured by HRTEM. Expanded scale used in the interval 0–2 nm, as evidenced by the arrow.

TABLE 6

Catalytic Activity in *n*-Heptane Dehydrocyclization[a] of Supported Palladium Catalysts vs Mean Particle Diameter

Catalyst	Pretreatment	Activity (%)[b,c]	Selectivity (%)[c] Toluene	Benzene	Mean particle diameter (Å)
Fresh Pd/MgO^{500}	H_2	70	24	51	6
Used Pd/MgO^{500}	O_2-H_2	60	29	47	18
Fresh Pd/MgO^{AIR}	H_2	11	40	32	61
Used Pd/MgO^{AIR}	O_2-H_2	10	40	31	125

[a] Experimental conditions: $T = 500°C$, $P = 1$ atm, $H_2/C_7H_{16} = 20$.
[b] Activity expressed as mole percent conversion of *n*-heptane to aromatics.
[c] Values taken after 60 min of time on stream.

on the activated magnesia, while for the MgO^{AIR} sample a wide diameter distribution is observed, centered at about 6.1 nm. On the silica support a broad distribution centered at about 9.9 nm is found.

After reduction–oxidation–reduction treatment of the magnesia-supported samples, the dispersion uniformity and size distribution shape are preserved, but larger particle mean diameters are obtained corresponding to about 1.8 and 12.5 nm, respectively.

3.5. Catalytic Activity

In the high-temperature dehydrocyclization reaction of *n*-heptane at atmospheric pressure, a fresh Pd/MgO^{500} catalyst, obtained by H_2 reduction of $Pd(acac)_2/MgO^{500}$ at 500°C, shows high activity (70%) and selectivity (80%) to formation of aromatics (benzene + toluene). The catalytic activity dramatically decreases when untreated MgO^{AIR} is used as a support (Table 6). However, the selectivity to toluene + benzene does not change significantly; the increase in benzene/toluene ratio is related to the increase in conversion. The low catalytic performance of the Pd/MgO^{AIR} sample is maintained on a conventional cycle of O_2 calcination and H_2 reduction at 500°C.

On Pd/MgO^{500} the regeneration simulation results in only a slight decrease in catalytic performance.

4. DISCUSSION

4.1. The Adsorption State

During the drying of the physisorbed sample on SiO_2^{450} and MgO^{AIR}, important rearrangements occur in the adsorbed layer, creating an interaction between the complex and the surface. Silica and untreated magnesia surfaces, as we are using here, should act primarily as a proton donor in H-bonding interactions, so it is unlikely that the adsorption interaction involves the acac methyl groups directly.

On silica the observed shifts in the symmetric and asymmetric stretching of C=O bonds (Fig. 2, Table 2) of the ligand, with out-of-plane vibrations of the ligand, are significantly perturbed by the proximity of the surface.

The interaction between silica surface and $Pd(acac)_2$ molecules is feeble; the impregnated precursor can be removed simply by washing with CH_2Cl_2, suggesting that the energy of interaction with the surface is similar to the solvation energy of the solvent. The disappearance or, better, the shift to higher wavenumber and the subsequent masking by other stronger bands of the bands assigned to o.o.p. bending of the C(3)–H bond (785 cm^{-1}) and its overtone (1550 cm^{-1}) could be due to mechanisms, either homogeneous or heterogeneous, involving band broadening, vibrational coupling, and energy transfer to the support, like those operating in the similar system $Cu(acac)_2/SiO_2$ (21), where the molecule interacts with the support lying with the molecular plane parallel to the surface. EXAFS data clearly show that the interaction with both the SiO_2 and MgO^{AIR} supports does not alter the structure of the molecule, as the coordination numbers and the distances from the Pd atom are the same as in the pure compound up to the higher ligand shells. Moreover, the inclusion of the path involving C_1 carbon atoms from adiacent molecules at the crystal distance produces a fit of much higher quality, as occurs for the pure crystal complex. This suggests the existence of $Pd(acac)_2$ crystallites on the support surface produced during impregnation, probably by precipitation.

After deposition with various amount of $Pd(acac)_2$, a fraction of the silanols is in hydrogen interaction with the quasi-π-system of the acac ligands, as shown by the broad IR band centered at about 3520 cm^{-1}. However, even at very high concentrations, a relatively large fraction of the free silanols remains unreacted on the silica surface. Therefore, it must be concluded that $Pd(acac)_2$ does not form a clean monolayer on the surface, but agglomerates forming "multilayered islands," leaving some parts of silica surface uncovered and other parts covered with precursor.

DRIFT spectra of chemisorbed $Pd(acac)_2$ on MgO^{500} show large positive shifts of the bands ascribed to symmetric stretching of C=O bond and double overtone of o.o.p. bending of C(3)–H; other bands are subjected only to minor shifts (Fig. 1c, Table 1). Since the active sites on MgO^{500} that can play a significant role in a chemisorption interaction are the basic O^{2-} ions, these shifts can be explained as the result of an ion–dipole-like interaction between oxide ions and carbon atoms of the carbonyl moiety of acetylacetonate, and to the formation of a hydrogen bond between oxide and hydrogen bound to C(3). It is noteworthy that the sign of the C=O shift is reversed with respect to those deriving from H bonding between halogenated solvent and carbonyl because in this case there is an electron donation

toward ligand. The large shift in 2γ(C–H) could also originate from the proximity of the molecule to the surface, which causes an asymmetry of the surrounding as reported in literature for the $Cu(acac)_2$–SiO_2 system; this explanation is consistent with the small shifts shown by the in-plane vibration of the same bond.

From EXAFS data it is evident that the number of oxygen and carbon atoms up to the fourth shell is unaffected by impregnation also on the activated magnesia, where the global peak reduced intensity is due only to increased structural disorder (Fig. 4, Table 3). The contributions from ligand higher shells indicate that the molecule has been anchored intact on the support surface. Interaction with the activated MgO support can be inferred from the presence of a great increase in the EXAFS disorder parameter in the molecule after chemisorption, which is more evident for the paths involving C_1 and C_2 carbon atoms. The structural disorder can be explained as due to the presence of many different sites on the MgO that, interacting with the absorbed molecules, cause a wider distribution of angles and distances than in the crystalline form. The fact that the disorder degree is higher for the more external carbon shells and the acetylacetonate ring bonds suggests that the interaction with the surface involves $-CH_3$ and –CH groups and a slight distortion of the ring. The absence of any contribution from the Pd–Mg shell up to the detectable distance range confirms the model of surface–complex interaction via ligands only.

4.2. Influence of the Adsorption State on Palladium Dispersion

A simple mechanism of reductive elimination of ligands is then expected to take place in hydrogen atmosphere, transforming the adsorbed complex into metal particles:

$$Pd(acac)_2/S + H_2 \rightarrow 1/nPd_n^0/S + 2acacH.$$

The thermal behavior was found to depend on two parameters: the nature of the adsorption state of the metal complex and the surface support. For SiO_2^{450}, the thermal decomposition proceeds via reductive elimination of ligands at 100°C (Fig. 3). The acetylacetone is partially evolved and partially retained by the porous silica surface at about 150°C. Subsequent reduction of the adsorbed ligand in close contact with the metal particles leads to a subsequent hydrogenation to 2,4-pentanediol, followed by 2-3 hydrogenolysis, giving 2-propanone, which is further reduced to 2-propanol. The evolution of methane at higher temperature is originated realistically by hydrogenation of carbonaceous residues left on the surface of metal particles during the previous decomposition of ligands, a process that is promoted by the presence of surface acidity (22).

For MgO^{AIR} (19), the evolution profile at low temperature is quite similar to those of $Pd(acac)_2$ on SiO_2^{450}, while the evolution of hydrogenated products, mainly 2-propanone, occurs at higher temperature than on silica surface (260°C vs 155°C), due to the fact that the untreated magnesia surface during the TPRD ramp partially restores its basic sites, on which the acetylacetonate adsorbs and undergoes a further 2-3 hydrogenolysis.

$Pd(acac)_2$ adsorbed on MgO^{500}, in contrast to samples supported on SiO_2^{450} and MgO^{AIR}, shows totally different thermal behavior (19). On activated magnesia the evolution of 2-propanone at low temperature (105°C) occurs via a 2-3 hydrogenolysis of ligand at the interface between the growing palladium particles and the MgO surface; instead, at higher temperature (290°C) 2-propanone derives from the decomposition of adsorbed carboxylates. Similar behavior has been reported for the decomposition of $Pd(acac)_2/Al_2O_3$, albeit under slightly oxidizing conditions (23) and is ascribed to the decomposition of acetylacetonate bound to c.u.s. Al^{3+}, leading to acetate and 2- propanone. The overall surface reactivity occurring at the interface adsorbed complex–support surface under TPRD conditions may be summarized as in Scheme 1.

The evolution of 2,4-pentanedione at low temperature on SiO_2^{450} and MgO^{AIR}, with respect to MgO^{500}, confirms the occurrence of a feeble interaction as suggested by EXAFS and IR data. In particular, the first-stage evolution that occurred at lower temperature on MgO^{AIR} than on SiO_2^{450} could be indicative of a simple physisorption of the palladium precursor without any significant chemical interaction with the surface, a magnesia with basic sites poisoned by surface carbonates.

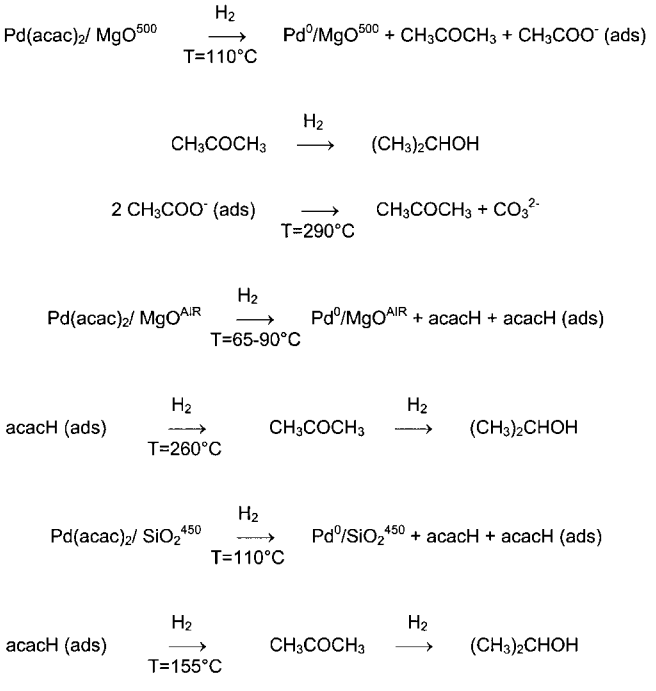

SCHEME 1

The metal phase developed on the support surface after hydrogen treatment at 500°C for each sample was characterized by EXAFS spectroscopy and HRTEM. Let us first compare the samples supported on MgO^{500} and SiO_2^{450}, which represent the two extremes of the adsorption state, while MgO^{AIR} shows intermediate behavior that depends also on the surface dynamical changes taking place during H_2 treatment. On MgO^{500}, the low Pd coordination number and the significant contribution of oxygen atoms (Table 5, Fig. 5), which after reduction are known to derive from the support only (as shown by the TPR analysis), reveal that the Pd particles are extremely small and interact strongly with the O^{2-} sites, as occurs under SMSI conditions (24). In the hypothesis of fcc structure and hemispherical cuboctaedric geometry, the first shell Pd coordination number corresponds to an average particle size of 8 Å. A shortening of the Pd–Pd bond length from 2.75 to 2.73 Å is also observed, as commonly reported in the literature for small metallic clusters, which are better described as molecules than as bulk metal. The high palladium dispersion is confirmed by HRTEM measurements (Fig. 6), which detect a mean diameters equal to 0.6 nm for the palladium particles.

At the other extreme, Pd/SiO_2^{450} after reduction shows no oxygen contribution and a high coordination number for Pd (Table 5) that is similar to that of bulk metal. In this case the presence of large particles with the fcc structure of metallic Pd is confirmed also by the presence of a relevant contribution from the higher shells. The particles have a mean diameter equal to 9.9 nm (Fig. 6).

On MgO^{AIR} the behavior is more complicated; actually the presence of the three Pd shells at the reported distances could be explained as resulting from a very disordered structure, suggesting the existence of a mixed metal and oxide phase. This hypothesis is suggested by the presence of a relevant oxygen contribution. It is known from the large evolution of water and carbon dioxide during the TPRD experiment that partial activation of MgO occurs during Pd reduction (25). This fact can account for the limitation of sintering to large Pd particles that "freeze" at an intermediate monolayer-like stage.

Any attempt to fit the Pd–Pd peak as a single or double shell with an asymmetric Debye–Waller factor failed. The observed distance distribution cannot be accounted for by a single or even double shell affected by a high degree of static disorder, but requires the presence of three distinct shells. A low palladium dispersion is obtained from the HRTEM data of this sample, with Pd particle mean diameter equal to 6.1 nm (Fig. 6), intermediate between those of the activated magnesia and silica-supported catalysts.

The properties of the metal phase obtained by H_2 treatment at 500°C are strongly dependent on the molecular precursor–support interaction: "the adsorption state." In the case of a weak interaction, the Pd precursor is not homogeneously distributed over the surface and the formation of highly dispersed metal particles is thus prevented.

4.3. Influence of Reduction–Oxidation–Reduction Treatments on Palladium Dispersion

EXAFS data show that the Pd/MgO^{500} sample, after oxidation treatment at 500°C, exhibits the formation of partially oxidized small Pd particles dispersed on the support (Table 5). The coordination number of 4.5 oxygen atoms indicates partial distortion with respect to the square planar coordination of four oxygen atoms around Pd of pure PdO, as a consequence of the strong interaction with the O^{2-} sites of magnesia. The Pd–Pd shell contribution is greatly reduced with respect to the coordination numbers of the bulk oxide, but the peak is still due to the sum of two close Pd shells in the same relative ratio as in the oxide, which proves the presence of small oxide crystallites interacting with the support.

HRTEM data show that when Pd/MgO^{500} undergoes an oxidation–reduction treatment, subsequent to the first reduction, the palladium particles so obtained have a mean diameter equal to 1.8 nm, with respect to the 0.6 nm of the freshly reduced sample. The EXAFS data after this second reduction do not indicate any particle enlargement effect, the coordination numbers and distances being the same as after the first reduction. Taking into account the experimental error, this could suggest the presence of still very small particles strongly interacting with the surface of the support. This discrepancy is due to the fact that EXAFS overestimates the smallest particle contribution, while in HRTEM the image contrast of the small metal particles with respect to the support decreases with particle size, making its detection more difficult. Anyway, even if the mean particle diameter is evaluated from the maximum of the HRTEM size distribution histogram only, the result indicates a good resistance of the very small magnesia-supported palladium particles to sintering. The small structural changes detected at the end of the reduction–calcination–reduction cycle, which simulates the regeneration treatment after a catalysis run, are in agreement with the catalytic behavior of the two samples, which show substantially unaltered activity before and after regeneration (Table 6).

On oxidation, the Pd/MgO^{AIR} sample leads to large PdO particles, as indicated by the relative intensity of the Pd–Pd shells, which perfectly reproduce the bulk oxide structure. A second reduction treatment following the oxidation produces metallic Pd particles that are larger than those after the first reduction, but still smaller than Pd particles on silica. The EXAFS parameters obtained still suggest the copresence of a metal and an oxide phase, but the contribution from the fcc structure of bulk metal Pd is now dominant with respect to the oxygen and Pd shells at distances corresponding to the PdO structure which are present to a smaller

extent. The Pd–Pd coordination number corresponding to the first metal shell is twice as large as after the first reduction, suggesting, in the hypothesis of hemispherical cuboctaedric geometry, a mean particle size of about 10 nm. Consistent with this value, the HRTEM histogram of the Pd/MgO^{AIR} sample after the oxidation–reduction treatments shows an increase in average particle size to 12.5 nm, with respect to the 6.1 nm of the freshly reduced sample. These results indicate a lower resistance to sintering of the relatively large supported metallic particles.

4.4. Catalysis of n-Heptane Dehydrocyclization

Catalysts containing noble metals (namely Pt and Pd) on basic supports are known to have high activity and selectivity to aromatics in the reforming reactions via a classic dehydrocyclization mechanism; they also show very low production of isomerization and cracking compounds owning to the absence of acid sites, as well as a very low deactivation rate. The high activity shown by the MgO^{500} samples, compared with the lower performance of the MgO^{AIR} samples, could be related to the different distributions of Pd particle size and, consequently, to interaction with surface basic sites of the support. According to Joyner *et al*. (26) the effect of the support on metal particle electron density is a short-range (<5 Å) effect. Consequently, the high activity of Pd/MgO^{500} catalyst is ascribed to the predominat fraction of very small particles in close contact with the basic sites of MgO support. Such interaction is then able to preserve the morphology of small metal particles and, therefore, the catalytic activity, on simulated high-temperature O_2/H_2 regeneration cycles.

The small fraction of active small Pd particles in Pd/MgO^{AIR} is thus responsible for the low performance of this material in terms of catalytic activity. The selectivity to aromatics is mantained, and the increase in toluene/benzene ratio is only a consequence of low conversion under catalytic conditions. Benzene is a secondary product in heptane dehydrocyclization, being formed from toluene by rupture of the weak benzylic CH_3 group. At low conversion toluene contact times are very low, reducing the proportion of toluene decomposition to benzene.

The regeneration treatment does not promote any beneficial effect on the low catalytic activity on Pd/MgO^{AIR} because the fraction of small palladium particles has not been increased, as confirmed by EXAFS and HRTEM data.

5. CONCLUSIONS

The aim of this work was the structural characterization of the surface chemistry of $Pd(acac)_2$ on different magnesia surfaces.

On MgO^{500} a strong chemisorption occurred, leading to dispersion at molecular level of the metallic complex. EXAFS confirms the model of surface–complex interaction via ligand only. In contrast, weak surface–complex interaction leads to the formation of islands of multilayers as observed for MgO^{AIR} and SiO_2^{450} surfaces.

The precursor–support interaction strongly influences the final properties of the metal phase: a well-dispersed, strongly bound precursor, as occurs on MgO^{500}, leads to a metal phase with similar properties; poorly interacting precursor molecules lead to large particles, as occurs on SiO_2^{450} and MgO^{AIR}.

We have demonstrated that the controlled reaction of organometallic compounds with surfaces of inorganic oxides is a necessary prerequisite to distribute the active phase in a highly dispersed form, and how this surface process is dependent on the nature of the adsorption state of the molecular precursor. It was also confirmed that small palladium particles in close contact with the basic sites of the support are the catalytic active species in the *n*-heptane dehydrocyclization.

ACKNOWLEDGMENTS

Financial support from CNR and MURST is gratefully acknowledged. We acknowledge the support and use of the facility of the LURE synchrotron laboratory in Orsay (Paris) and thank the staff of the XAS-13 beamline for their assistance. We thank Professor Coluccia for access to the HRTEM instrument of the IFM Chemistry Department of Torino University.

REFERENCES

1. Yermakov, Y. I., Kuznetsov, B. N., and Zacharov, V. A., *in* "Catalysis by Supported Complexes," Stud. Surf. Sci. Catal., Vol. 8, Ch. 9, p. 305, Elsevier, Amsterdam, 1981; Köhler, S., Reiche, M., Frobel, C., and Baerns, M., *in* "Preparation of Catalysts VI: Scientific Bases for the Preparation of Heterogeneous Catalysts" (G. Poncelet, *et al*., Eds.), p. 1009, Elsevier, Amsterdam, 1995; Locatelli, F., Didillon, B., Uzio, D., Niccolai, G., Candy, J. P., and Basset, J. M., *J. Catal.* **193**, 154 (2000).
2. Boitiaux, J. P., Cosyns, J., and Vasudevan, S., *Appl. Catal.* **6**, 41 (1983).
3. Lesage-Rosemberg, E., Vlaic, G., Dexpart, H., Lagarde, P., and Freund, E., *Appl. Catal.* **22**, 211 (1986).
4. van Veen, J. A. R., Jonkers, G., and Hesselink, W. H., *J. Chem. Soc. Faraday Trans.* **85**(2), 389 (1989).
5. Mares, F., Galla, J. E., Diamond, S. E., and Regina, F. J., *J. Catal.* **112**, 145 (1988); Davis, R. J., and Derouane, E. G., *Nature* **349**, 313 (1991); Recchia, S., Dossi, C., Poli, N., Fusi, A., Sordelli, L., and Psaro, R., *J. Catal.* **184**, 1 (1999).
6. Dossi, C., Fusi, A., Recchia, S., Anghileri, M., and Psaro, R., *Chem. Commun.*, 1245 (1994).
7. Kappers, M., Dossi, C., Psaro, R., Recchia, S., and Fusi, A., *Catal. Lett.* **39**, 183 (1996).
8. Psaro, R., Dossi, C., and Ugo, R., *J. Mol. Catal.* **21**, 331 (1983).
9. "Gmelin Handbuch der Anorganischer Chemie," Palladium, p. 302. Verlag Chimie, Weinheim, 1947.
10. Primet, M., Basset, J. M., Mathieu, M. V., and Prettre, M., *J. Catal.* **28**, 368 (1973).
11. Dossi, C., Fusi, A., and Psaro, R., *Thermochim. Acta* **236**, 165 (1994).
12. Dossi, C., Fusi, A., and Russo, O., *Anal. Eur.*, 17, April 1995.

13. Report of the International Workshop on Standards and Criteria in XAFS, *in* "X-Ray Absorption Fine Structure" (S. S. Hasnain, Ed.), p. 751. Hellis Horwood, Chichester, 1991.
14. Michalowicz, A., *J. Phys. IV Fr.*, 7C2-235 (1997).
15. Lengeler, B., and Eisenberger, E. P., *Phys. Rev. B* **21**, 4507 (1980).
16. James, F., and Roos, M., *Comput. Phys. Commun.* **10**, 343 (1975).
17. Mustre de Leon, J., Rehr, J. J., Zabinsky, S. I., and Albers, R. C., *Phys. Rev. B* **44**, 4146 (1991); Zabinsky, S. I., Rehr, J. J., Ankuninov, A., Albers, R. C., and Eller, M. J., *Phys. Rev. B* **52**, 2995 (1995).
18. Vlčková, B., Struch, B., and Horák, M., *Collect. Czech. Chem. Commun.* **50**, 306 (1985).
19. Dossi, C., Psaro, R., Fusi, A., Recchia, S., Dal Santo, V., and Sordelli, L., *Thermochim. Acta* **317**, 157 (1998).
20. Joyner, R. W., Martin, K. H., and Meehan, P., *J. Phys. C* **20**, 4005 (1987).
21. Mitchell, M. B., Chacravarthy, V. R., and White, M. G., *Langmuir* **10**, 4523 (1994).
22. Dossi, C., Psaro, R., Sordelli, L., Bellatreccia, M., and Zanoni, R., *J. Catal.* **159**, 453 (1996); Bell, A. T., *Stud Surf. Sci. Catal.* **48**, 91 (1989).
23. van Veen, J. A. R., Jong-Versloot, MS. P. C., Van Kessel, G. M. M., and Feels, F. J., *Thermochim. Acta* **152**, 359 (1989).
24. Kappers, M., Dossi, C., Psaro, R., Recchia, S., and Fusi, A., *Catal. Lett.* **39**, 183 (1996).
25. Anderson, P. J., Horlock, R. F., and Oliver, J. F., *Trans. Faraday Soc.* **61**, 2754 (1965).
26. Joyner, R. W., Pendry, J. B., Saldin, D. K., and Tennison, S. R., *Surf. Sci.* **138**, 84 (1984).